Optimizing Satellite-Based Latent Heating Rate Profiling Using a Convolutional Neural Network Heating (CNNH) Algorithm

Hongwei Zhao, Shuping Yang, Qiong Wu, Lin Chen, Peng Zhang, *Senior Member, IEEE*, and Rui Li

***Abstract*— Precise spatial distribution of latent heat released during precipitation formation is crucial to enhance weather forecasting and climate prediction accuracy. This study introduces an innovative convolutional neural network heating (CNNH) algorithm. The algorithm incorporates the vertical gradient of precipitation rate and air temperature at different altitudes as key inputs. It combines additional information from adjacent vertical layers and neighboring horizontal areas. To mitigate possible misjudgments of negative heating, a punishing mechanism was introduced with a latent heating (LH)-structure loss function within the optimization framework. By employing the adaptive differential evolution (ADE) algorithm, the optimal configuration of the network structure optimizes accurate LH retrieval. To evaluate the CNNH algorithm's efficacy, a self-consistency check using weather research and forecasting (WRF) model simulation data was conducted. Furthermore, an intercomparison study with four other algorithms using real satellite observations was undertaken. Evaluations found that the CNNH algorithm could precisely retrieve the primary characteristics of the horizontal and vertical structure, along with the temporal evolution process and statistical information of WRF simulated LH, in eastern China in August 2017. It effectively addressed the issues of overestimation of near-surface cooling and mixing layer heating, thereby outperforming selected artificial intelligence (AI) and physics-based LH algorithms. The intercomparison study between LHCNNH with four other published LH products based on the same GPM observations reveals that CNNH got comparable performance among them. However, specific differences among these algorithms highlight considerable uncertainties in multiple LH satellite remote sensing products and underscore the necessity for further improvements in satellite LH algorithms.**

***Index Terms*— Convolutional neural network (CNN), horizontal neighborhood information, latent heat, satellite remote sensing, structure information.**

Received 21 July 2024; revised 6 September 2024 and 12 September 2024; accepted 14 September 2024. Date of publication 25 September 2024; date of current version 9 October 2024. This work was supported in part by the National Natural Science Foundation of China NSFC under Grant 42330602, Grant 42275139, and Grant 41830104; in part by Anhui Provincial Natural Science Foundation under Grant 2208085UQ02; in part by the National Key Research and Development Program of China under Grant 2021YFC3000300; in part by the Innovation Center for Fengyun Meteorological Satellite Special Project under Grant FY-APP-ZX-2022.0211; in part by CMA-USTC Laboratory of Fengyun Remote Sensing; and in part by the Youth Innovation Team of the "Fengyun Satellite Remote Sensing Product Verification" of the China Meteorological Administration under Grant CMA2023QN12. *(Corresponding author: Rui Li.)*

Hongwei Zhao and Shuping Yang are with the School of Earth and Space Sciences, University of Science and Technology of China, Hefei 230026, China (e-mail: hwzhao@ustc.edu.cn; shupi@mail.ustc.edu.cn).

Qiong Wu and Lin Chen are with the National Satellite Meteorological Center, China Meteorological Administration, Beijing 10008l, China (e-mail: wuqiong@cma.gov.cn; chenlin@cma.gov.cn).

Peng Zhang is with the Meteorological Observation Centre, China Meteorological Administration, Beijing 100081, China (e-mail: zhangp@cma.gov.cn).

Rui Li is with the School of Earth and Space Sciences, State Key Laboratory of Fire Science, MEM Key Laboratory of Forest Fire Monitoring and Warning, CMA-USTC Laboratory of Fengyun Remote Sensing, University of Science and Technology of China, Hefei 230026, China (e-mail: rli7@ustc.edu.cn).

Digital Object Identifier 10.1109/TGRS.2024.3466952

NOMENCLATURE

LH	Latent heating.
ADE	Adaptive differential evolution algorithm.
WRF	Weather research and forecasting model.
CRM	Cloud-resolving model.
GPROF	Goddard profiling heating algorithm.
MWRT	Microwave radiative transfer model.
GPM	Global precipitation measurement.
DPR	Dual-frequency precipitation radar.
CNN	Convolutional neural network.
LUTs	Look-up tables.
FE-Module	Feature extraction module.
Fu-Module	Fusion module.
Reg-Module	Regression module.
Rr	Rain rate.
CSH	Convective-stratiform heating algorithm.
SLH	Spectral latent heating algorithm.
CNNH	Convolutional neural network heating algorithm.
FCNH	Fully connected neural network heating.
VPH	Vertical profile heating algorithm.
LH_{WRF}	LH simulated by the WRF model.
LH_{CNNH}	LH retrieved by the CNNH method.
LH_{FCNH}	LH retrieved by the FCNH algorithm.
LH_{VPH}	LH retrieved by the VPH algorithm.
LH_{SLH}	LH retrieved by the SLH algorithm.
LH_{CSH}	LH retrieved by the CSH algorithm.
Ccr	Concordance correlation coefficient.
RMSE	Root mean square error.
MAE	Mean absolute error.

I. INTRODUCTION

LH RELEASED in the cloud is a result of the water phase transition among gas, liquid, and solid, and the LH

serves as the main energy source driving atmospheric large-scale circulations [1], [2], [3], [4]. Meanwhile, global/local atmospheric circulations also feedback on the horizontal and vertical distribution of LH [5], [6]. LH can play a significant role in aerosol-cloud-precipitation interactions, influence cloud lifecycle and precipitation intensity [7], [8], promote deep convection development, and regulate the climate-energy balance. Quantitative analysis of the horizontal and vertical distribution of LH is crucial for understanding the feedback of atmospheric circulation, clouds, and precipitation to climate change [9]. However, LH cannot be measured directly [10]. The development of accurate methods for the retrieval of LH is particularly important.

Satellite remote sensing of LH mainly relies on the measurements of vertical profiles of precipitation rate. Internationally recognized LUT methods for retrieving LH include the CSH algorithm [11], [12], the SLH algorithm [13], [14], [15], and the GPROF algorithm [16]. These methods share a similar approach, which involves using satellite observable parameters as indices to find the best estimation in an LUT that contains a large number of LH profiles simulated and constructed based on a CRM and MWRT model. The CSH algorithm [11], [12], [17] was developed based on the finding that LH profiles are highly dependent on the surface rain rate and rain type of the convective and stratiform precipitation. In recent years, the CSH algorithm has further developed and utilized the average echo top height and the low-level vertical reflectivity gradient to estimate the heating depth and low-level evaporation cooling intensity in stratiform regions [18]. Additionally, Tao et al. [19] used CRM simulations of three different weather events over the eastern continental United States and three different events over the western coast to construct LUTs suitable for high-latitude and cold-season LH retrieving and compared and analyzed different versions of CSH LH products [20]. The SLH algorithm [13], [14], [15], [21], [22] is also an LUT-based method that considers not only the rain top height as an indicator of LH release rate but also factors such as rain type, surface rainfall rate, and freezing layer height as important indices on LH. It constructs an LUT by representing the LH profiles as functions of the aforementioned variables obtained from CRM simulations. The GPROF algorithm uses the Bayesian retrieving method to find the best estimation of LH based on multiple channel brightness temperature upwelling from the top of the atmosphere, which was measured by satellite and CRM-MWRT simulations.

The advantages of the above LUT algorithms are that they can fully reflect the various components of LH released by precipitation (condensation–evaporation, freezing–melting, deposition–sublimation) and other atmospheric heating, including radiation heating, and can also estimate the LH of non-precipitating clouds. However, the retrieving accuracy of these algorithms is highly dependent on the representativeness and completeness of the pre-established LUTs.

Physical-based LH algorithms are used to estimate LH based on the physical relationship between observable clouds and precipitation characteristics from satellite and LH. Assuming that the storm is in a steady state, the net flux of local hydrometeors is compensated through its phase change process (reduced or increased), and the phase change of hydrometeors releases LH that heats (or cools) the atmosphere. Based on this assumption, Tao et al. [23] proposed an LH retrieving method based on the vertical profile of hydrometeors. Inspired by this work, other LH retrieving methods based on hydrometeor profiles have been subsequently proposed, such as the HH algorithm [24], [25], [26] and the PRH algorithm [27].

Through further research and analysis of the precipitation rate profile, it was found that the vertical gradient of precipitation rate represents the microphysical processes of different phase transitions of water, corresponding to different LH releasing rates [28], [29]. Li et al. [30] concluded that under certain assumptions, the vertical gradient of a precipitation profile can be approximated as a first-order approximation of precipitation growth rate and LH releasing rate. Min et al. [31] and Li et al. [32] analyzed different types of precipitation and their involvement in different phase transition processes and estimated LH using cloud water content and precipitation rate. Based on the aforementioned studies, Li et al. [33] hypothesized that newly formed cloud water in precipitation clouds converts to rainwater at the same rate, and the precipitation rate profile remains stable in a short period. They derived that the vertical gradient of precipitation rate is proportional to the LH release rate and thus proposed a physically-based algorithm for LH retrieval from precipitation profiles called the Vertical profile heating (VPH) algorithm. The LH is expressed as a piecewise linear function of the vertical gradient of the precipitation profile. To reduce the errors caused by these assumptions, Li et al. [33] also designed additional corrections. The VPH algorithm was validated for consistency using cloud simulations from WRF models, and its performance was evaluated through satellite observations from the GPM-DPR over the Qinghai-Tibet Plateau, showing reasonable results. Moreover, in this work, Li et al. [33] verified that the vertical gradient of rain rate itself can reflect the differences in precipitation formation rates among different precipitation types, and there is a high correlation between the vertical gradient of rain rate and LH in both horizontal distribution and vertical profile.

According to previous studies by Li et al. [30], [32], [33], there is a strong physical relationship between the vertical profile of rain rate and LH. However, In the VPH algorithm, the highly nonlinear relationship between the observation of precipitation parameters and the LH rate is greatly simplified. Artificial intelligence (AI) methods can effectively learn to describe nonlinear relationships between input and output variables. In the previous work [34], we attempted to retrieve LH using artificial neural networks for the first time and proposed an LH retrieving algorithm based on FCNHs, which effectively improved the retrieving accuracy. However, the existing physical-based research and AI method still have several limitations, as follows.

1) Studies have shown that horizontal advection of atmospheric motion leads to displacement between the growth of precipitation particles

and the condensation/evaporation phase change of hydrometeors [30]. However, existing LH retrieving methods only interpret the vertical differential of precipitation rate as an increase or decrease of precipitation particles in the vertical direction, neglecting the influence of horizontal displacement of hydrometeors.

2) Under the influence of actual atmospheric motion, precipitation particles fall out of the cloud and undergo microphysical processes such as melting, sublimation, and evaporation until reaching the surface, forming a coherent profile of precipitation rate [35]. However, existing studies merely calculate the vertical gradient of precipitation rate for spatially local grid points when estimating LH, thereby losing the overall vertical structural information of the precipitation rate profile, which is not conducive to accurate LH retrieving.

CNNs can capture both local and global information across multiple dimensions, and they have achieved significant success in various tasks within the domain of remote sensing of the cloud and precipitation. Sadeghi et al. [36] employed a U-shaped CNN to extract and integrate infrared observational data and geographical information, thereby enhancing the accuracy of near-real-time precipitation estimation. Tu et al. [37] combined the WRF model with a CNN, leveraging the network's ability to extract regional and global features from WRF simulation data, enabling downscaling from ERA-Interim dataset resolutions of 80–6 km. Niu et al. [38] structured radar echo, temperature, and total precipitation data into a 3-D format, utilizing CNN for multi-variable feature extraction and integration, thus achieving heightened precision in precipitation prediction. King et al. [39] developed a CNN-based remote sensing precipitation retrieval model capable of estimating average surface precipitation within 20-min intervals, showcasing the superiority of the CNN model over conventional machine learning algorithms. Jing et al. [40] introduced an attention mechanism-based CNN approach and applied it to the downscaling of satellite-derived precipitation data, refining the resolution of GPM IMERG monthly precipitation records from $0.1^\circ \times 0.1^\circ$ to $0.01^\circ \times 0.01^\circ$.

In summary, CNNs have indeed accumulated a commendable track record in the application of satellite remote sensing for clouds and precipitation. However, to the best of our knowledge, although CNNs have strong nonlinear fitting and feature extraction capabilities, there has not yet been any exploration of using CNNs specifically for the retrieval of LH.

In order to improve the retrieving accuracy of LH, this study incorporates the horizontal neighborhood information and the vertical profile structure of hydrometeors as prior knowledge and combines them with the powerful feature extraction ability of CNNs to propose a 3-D CNN-based LH retrieving method (CNNH). Additionally, an ADE algorithm [41] is used to obtain the optimal hyperparameters of the CNNH network to further enhance the model performance. Moreover, in the design of the loss function, in addition to using the classical mean squared error (mse) loss, this study incorporates the LH structure loss based on the characteristics of LH to guide model training. Compared to VPH and FCNH algorithms on WRF-simulated data, the proposed method significantly improves the accuracy of LH retrieving. Furthermore, the CNNH retrieving results of LH are compared and analyzed with those obtained from the FCNH, VPH, SLH, and CSH algorithms using GPM DPR observation data.

II. Datasets

A. GPM DPR Data

The GPM satellite, launched on February 28, 2014 [42], carries the GPM DPR onboard. It provides 3-D observations of radar reflectivity of precipitation particles within the range of 65°S–65°N globally. The GPM DPR operates at frequencies of 13.6 GHz (Ku bands) and 35.5 GHz (Ka bands), with a horizontal resolution of approximately 5.2 km and a vertical sampling interval of 0.125 km at nadir. In this study, we utilize the GPM DPR Level 2 product, 2ADPR [43], for case studies to evaluate our LH retrieving results. In addition, GPM standard product 2ADPR ENV was used to provide air temperature T in the retrieval process. The spatiotemporal resolution of 2ADPR ENV is consistent with that of 2ADPR.

2HSLH and 2HCSH, official GPM LH products, were used for comparison with the retrieval of the CNNH algorithm. The 2HSLH and 2HCSH products have a horizontal resolution of 5.2 km and a vertical resolution of 0.25 km. These data can be downloaded from NASA.

B. CRM Simulations

Cloud-resolving model simulations have been widely used to develop LUTs for LH retrieving algorithms, especially when actual measurements are not available. As one of the most used mesoscale numerical models, the WRF model [44], [45] considers detailed geographical information, including terrain, in its preprocessing system. In this study, the Advanced Research WRF model Version 3.4 (referred to as WRF) was employed to simulate clouds in the research area (32°N–55°N, 105°E–131°E) in August 2017. The simulations were conducted using two nested domains with inner and outer spatial resolutions of 3 and 9 km, respectively. The output data included 55 vertical levels (with a vertical resolution of 0.25 km below 5 km) and a horizontal resolution of 4 km, with output saved every 0.5 h. Since WRF does not directly output LH, this study utilized the phase changes of all hydrometeors outputted by WRF to calculate LH.

The configuration of physical schemes employed within the WRF model is structured as follows: the Thompson scheme [46] was used as the microphysical parameterization, and radiation processes are simulated using both the RRTMG longwave and shortwave schemes [47]. Near-surface processes rely on a revised version of the MM5 scheme [48], while land surface interactions are managed by the Unified Noah land surface model [49]. The boundary layer dynamics are governed by the YSU planetary boundary layer scheme [50]. Convective processes are parameterized through the Grell–Freitas scheme [51], implemented exclusively in the outer model domain; hence, no convective parameters are specified for the inner domain. To initialize and provide boundary conditions, the model harnesses global

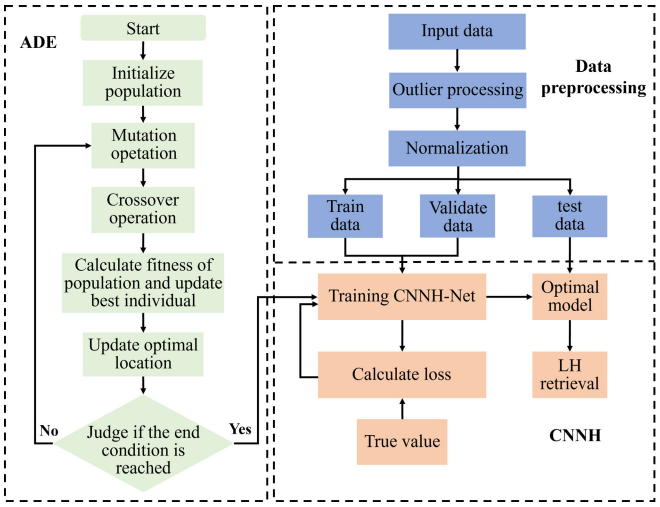

Fig. 1. Flowchart of CNNH method.

reanalysis data from the National Centers for Environmental Prediction [52].

During the simulation, the WRF model generated output data at intervals of 30 min. For the training phase of the FCNH network, nine time steps were arbitrarily chosen from these outputs to constitute the training dataset, with all remaining output data allocated for the testing dataset.

The Acronyms in this study are provided in Nomenclature.

III. LH Retrieval Algorithm Based on 3-D CNNH

A. Method Overview

Fig. 1 depicts the overall flowchart of the CNNH method. First, the original data is preprocessed, the outliers are eliminated, and the normalization is carried out. Second, the data is divided into training sets, verification sets, and test sets and sent to the constructed CNNH-net for model training and testing. Simultaneously, the ADE algorithm is employed to intelligently optimize the network hyperparameters, resulting in the optimal design of network parameters.

B. Data Preprocessing

In order to enhance the efficiency of model training, data cleaning was performed. The vertical derivation of rain rate ($\Gamma = -dRr/dz$) and LH below the surface were assigned a value of 0, while the temperature below the surface was assigned the temperature of the surface layer. Any other outliers were filled using the mean value of the surrounding neighboring data.

To eliminate the dimensional impact between data, it is necessary to perform data standardization. We applied the min-max normalization technique to normalize each variable, as shown in the following equation:

$$x^* = \frac{x - x_{\min}}{x_{\max} - x_{\min}} \tag{1}$$

where, x and x^* indicate the value of the variable and the normalized value of the variable, respectively. $x_{\max}$ and $x_{\min}$ indicate the maximum and minimum value of the variable in the dataset, respectively.

C. Construction of the CNNH Network

Fig. 2 presents the architecture of the CNNH network. The network consists of three components: the FE-Module, the Fu-Module, and the Reg-Module. The specific configuration of the network is shown in Table I. Initially, the input information undergoes feature extraction through the FE-Module, followed by feature fusion through the FE-Module. Finally, the Reg-Module processes the fused features to obtain the retrieved LH.

The FE-Module was designed to extract features from the input variables. Let the two inputs $X_{1,(i,j)} = \Gamma_{(i,j)} = \{-(dR_{(i,j,k)}/dz_{(i,j,k)})|k = 1, \ldots, l\}$ and $X_{2,(i,j)} = T_{(i,j)} = \{T_{(i,j,k)}|k = 1, \ldots, l\}$ represent the vertical derivative profile of the rain rate profile ($\Gamma = -dRr/dz$) and the air temperature profile (T) at horizontal coordinates (i, j), and l represents the number of vertical layers in the rain rate profile. Taking into account the horizontal and vertical information from neighboring area and adjacent layers, let $\Gamma^r_{(i,j)} = \{-(dR_{(i,j,k)}/dz_{(i,j,k)})|k = 1, \ldots, d$ and (i, j) in $r\}$ and $T^r_{(i,j)} = T_{(i,j,k)}|k = 1, \ldots, d$ and (i, j) in $r\}$ represent all vertical gradient of rain rate profiles and temperature profiles in a neighborhood radius r centered on coordinates (i, j) and layers from 1 to d ($d = 65$). Let $x_{s,(i,j)}$ represent the profile information of the sth variable, then the output of the nth block in the FE-Module can be mathematically expressed as follows:

$$z^n_{s,(i,j)} = \begin{cases} \mathrm{ReLU}\left(f^n_{\mathrm{conv3D}}\left(x_{s,(i,j)}\right)\right), & n = 1 \\ \mathrm{MP}\left(\mathrm{ReLU}\left(f^n_{\mathrm{conv3D}}\left(z^{(n-1)}_{s,(i,j)}\right)\right)\right), & n \text{ is even and } n < p \\ \mathrm{ReLU}\left(f^n_{\mathrm{conv3D}}\left(z^{(n-1)}_{s,(i,j)}\right)\right), & n \text{ is odd and } n < p \end{cases} \tag{2}$$

$$f^n_{\mathrm{conv3D}} = \mathrm{conv3D}\left(W^n, B^n, \mathrm{kernal\_size} = (3,3,3), \mathrm{stride} = (1,1,1), \mathrm{padding} = \mathrm{same}\right) \tag{3}$$

$$\mathrm{ReLU}(x) = \max(0, x) \tag{4}$$

$$\mathrm{MP}(x) = \mathrm{Maxpool}(x) \tag{5}$$

where f^n_{conv3D} represents the 3-D convolution layer of the nth block, W and B represent the weight and bias to be learned, respectively, kernal_size is the size of the convolution kernel, stride is the step of the convolution operation, setting padding to "same" means that the convolution operation maintains the input and output size unchanged, ReLU$(\cdot)$ is used as the activation function, and p represents the maximum number of blocks contained in the FE-Module. Then, the final output of each FE-Module can be expressed as $z^p_{s,(i,j)}$.

The Fu-Module integrates and further extracts features derived from individual variables, having a network configuration similar to the FE-Module, consisting of two submodules. The first submodule incorporates a single 3-D convolutional layer followed by a ReLU activation function, while the second submodule includes another 3-D convolutional layer, a ReLU activation layer, and an average pooling layer. Taking the output from the FE-Module as the input to the Fu-Module, the subsequent fusion and advanced feature

representation result in

$$F^n_{(i,j)} = \begin{cases} \mathrm{ReLU}\left(f^n_{\mathrm{conv3D}}\left(\left[z^{(p)}_{1,(i,j)}, z^{(p)}_{2,(i,j)}\right]\right)\right), & n = p+1 \\ \mathrm{AP}\left(\mathrm{ReLU}\left(f^n_{\mathrm{conv3D}}\left(F^{(n-1)}_{(i,j)}\right)\right)\right), & n = p+2 \end{cases} \tag{6}$$

$$\mathrm{AP}(x) = \mathrm{Avgpool}(x). \tag{7}$$

The Reg-Module performs regression predictions on the fused features; differing from the FE-Module and the Fu-Module, the Reg-Module is designed as a fully connected network. The output of its layers can be expressed as

$$R^n_{(i,j)} = \begin{cases} \mathrm{ReLU}\left(h_{w^n,b^n}\left(F^{p+2}_{(i,j)}\right)\right), & l = p+3 \\ \mathrm{AP}\left(\mathrm{ReLU}\left(h_{w^n,b^n}\left(D^{n-1}_{(i,j)}\right)\right)\right), & l = q. \end{cases} \tag{8}$$

Then, the retrieved LH of precipitation at coordinates (i, j) can be expressed as

$$\mathrm{LH}^{(i,j)}_{\mathrm{ret}} = R^q_{(i,j)} \tag{9}$$

where q represents the total number of blocks contained within the Reg-Module network. $h(\cdot)$ denotes the linear regression function, and w and b represent the weight and bias to be learned, respectively.

To investigate the influence of hydrometeor horizontal displacements and vertical advection on LH retrieval performance, this study not only employs the designed 3-D CNN for LH retrieval but also juxtaposes the effectiveness of LH retrieval via 1-D and 2-D CNNs. In the context of the 1-D CNN-based LH retrieval method, the input consists solely of the vertical profiles of the variables, devoid of any horizontal contextual information. On the other hand, the 2-D CNN-based approach to LH retrieval considers only the horizontal contextual information, excluding any vertical information of precipitation.

D. Loss Function

The decrease of precipitation rate toward the surface (i.e., $\Gamma < 0$) was simply regarded as evaporation, thus negative LH (cooling) [30], [33]. However, this is not necessarily the case in the real cloud. Breaking up of rain drops, horizontal advection, the slant-view angle of precipitation radar, etc., can all cause observed negative Γ. To punish such misjudgment during the machine learning process, an additional LH-structure loss (L_{str}) was introduced alongside the standard RMSE loss in our optimization framework. The calculation formula for the Loss is as follows:

$$\mathrm{Loss} = \omega \times L_{\mathrm{RMSE}} + (1-\omega) \times L_{\mathrm{str}} \tag{10}$$

$$L_{\mathrm{RMSE}} = \sqrt{\frac{1}{N}\sum_{i=1}^{N}(\mathrm{LH}_{\mathrm{ret}i} - \mathrm{LH}_{\mathrm{mod}i})^2} \tag{11}$$

$$L_{\mathrm{str}} = \frac{1}{N}\sum_{i=1}^{N}(1 - \mathrm{sgn}(\mathrm{LH}_{\mathrm{ret}i} \times \mathrm{LH}_{\mathrm{mod}i})) \times |\mathrm{LH}_{\mathrm{ret}i} - \mathrm{LH}_{\mathrm{mod}i}| \tag{12}$$

where $\mathrm{LH}_{\mathrm{mod}}$ and $\mathrm{LH}_{\mathrm{ret}}$, respectively, denote the WRF-modeled LH and retrieval LH, N represents the number of samples, and ω represents a balance coefficient which has a range of [0, 1]. In (12), if $\mathrm{LH}_{\mathrm{mod}}$ and $\mathrm{LH}_{\mathrm{ret}}$ have the same sign, then $L_{\mathrm{str}} = 0$; if $\mathrm{LH}_{\mathrm{mod}}$ and $\mathrm{LH}_{\mathrm{ret}}$ have different sign, the $L_{\mathrm{str}} = (1/N)\sum_{i=1}^{N} |\mathrm{LH}_{\mathrm{ret}i} - \mathrm{LH}_{\mathrm{mod}i}|$, and the loss L_{str} will increase as the difference between $\mathrm{LH}_{\mathrm{ret}}$ and $\mathrm{LH}_{\mathrm{mod}}$ increases.

E. ADE Algorithm

Intelligent optimization algorithms have been proven to effectively configure the hyperparameters of deep learning models [53]. The ADE algorithm [54] was adopted to adjust the hyperparameters of CNNH, a strategy known for adeptly maintaining a balance between explorative reach and convergence velocity, ensuring swift and effective navigation toward the global optima. In this study, the pivotal hyperparameters for the CNNH model include the learning rate (l_r), the number of hidden layers in the FE-Module (N_{FE}), the number of units in hidden layer channels in the FE-Module (n_{FE}), the number of hidden layers in the Reg-Module (N_{Reg}), and the number of units in hidden layer channels in the Reg-Module (n_{Reg}). The steps to optimize the hyperparameters of CNNH using the ADE algorithm are as follows:

Step 1: Initialization of Population. A population of size M is initialized, where each individual $x_i = [l_r, N_{\mathrm{FE}}, n_{\mathrm{FE}}, N_{\mathrm{Reg}}, n_{\mathrm{Reg}}]$, then the genetic dimension $D = 5$. Each gene j has a value range $[L_j, U_j]$. Obtain the initial population using the following formula:

$$x_{i,j} = L_j + \mathrm{rand}(0,1) * (U_j - L_j) \quad i = 1, 2, \ldots, M; \quad j = 1, 2, \ldots, D. \tag{13}$$

Step 2: Mutation Operation. For each individual, a mutation operation is performed. x_{r1} and x_{r2} are randomly selected individuals in the population. Set the maximum number of iterations as T, t denotes the current iteration count, and the mutation operator is F, with its value ranging within [0, 1]. Notably, the mutation strength decreases as the iteration progresses. During the early stages of the algorithm, a larger mutation factor ensures population diversity, aiding in the search for global optima. In the later stages, a smaller mutation factor is employed to preserve excellent individuals, exhibiting stronger local search capability and ensuring convergence of the algorithm. Following the mutation operation, the individual v_i is expressed as:

$$v_i = x_i + F * (x_{r1} - x_{r2}) \tag{14}$$

$$F = F_{\min} + (F_{\max} - F_{\min}) * \frac{1}{1 + e^{10(t-0.5*T)/T}}. \tag{15}$$

Step 3: Crossover Operation. Set crossover probability as CR, with its value ranging within [0, 1]. A crossover individual, denoted as u_i, is generated through the process of crossing the current individual with the mutated one. The genes of the crossover individual are selected according to the following equation:

$$u_{i,j} = \begin{cases} v_{i,j}, & \text{if } \mathrm{rand}(0,1) \le CR \\ x_{i,j}, & \text{otherwise.} \end{cases} \tag{16}$$

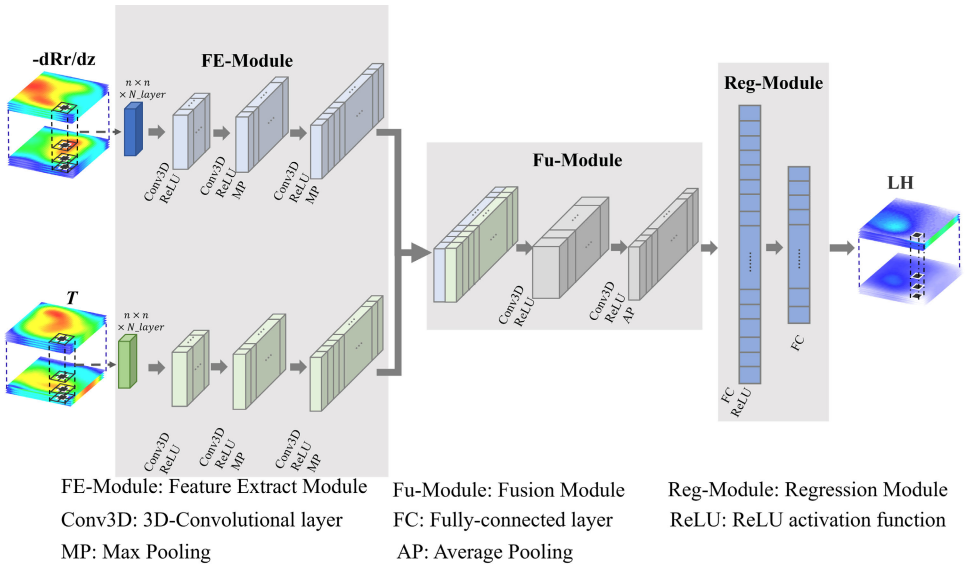

Fig. 2. Illustration overview of CNNH framework for LH retrieval.

TABLE I
CNNH NETWORK CONFIGURATION

Input	FE-Module				Fu-Module		Reg-Module		Output
	Block1	Block2	Block3	Block4	Block5	Block6	Block7	Block8	
$m \times 5 \times 5 \times l$	$3 \times 3 \times 3$ Conv	$3 \times 3 \times 3$ Conv	$3 \times 3 \times 3$ Conv	$3 \times 3 \times 3$ Conv	$1 \times 1 \times 1$ Conv	$1 \times 1 \times 1$ Conv	FC	FC	l
	ReLU	ReLU	ReLU	ReLU	ReLU	ReLU	ReLU	-	
	-	MP	-	MP	-	AP	-	-	
	$16 \times 5 \times 5 \times l$	$32 \times 3 \times 3 \times l$	$64 \times 3 \times 3 \times l$	$128 \times 2 \times 2 \times l$	$128 \times 2 \times 2 \times l$	$64 \times 1 \times 1 \times l$	$32 \times l$	l	

*Conv, ReLU, MP, AP, and FC represent the convolution layer, ReLU activation function, Max-Pooling, Average-Pooling, and Fully connection layer respectively; m represents the number of input features; l represents the number of layers contained in vertical profile. In addition, the last group of data for each Block represents the output size

Step 4: Selection Operation. The target individual y_i is selected according to the fitness

$$y_i = \begin{cases} u_i, & \text{if } g(u_i) \le g(x_i) \\ x_i, & \text{otherwise} \end{cases} \tag{17}$$

where the fitness $g(\cdot) = 1/\text{loss}$, and the loss represents the value of the Loss of neural network under the current hyperparameter settings. If the maximum number of iterations is not reached, jump to step 2; if the number of iterations reaches the maximum number, terminate the iteration and output the individual with the highest fitness value as the final setting of the hyperparameter.

IV. RETRIEVING LH USING WRF-MODELED DATA

To develop the CNNH algorithm, particularly to test the sensitivity of the algorithm to precipitation information in horizontal neighboring areas and in vertically adjacent layers, case study and statistical study and testing were conducted with CRM simulations, which were regarded as ground truth.

A. Case Study

Figs. 3–5 show a precipitation event at UTC 12:30 on August 27, 2017. Fig. 3 presents the horizontal distribution of surface precipitation rates, the vertical gradient of rain rate ($-dRr/dz$), and simulated LH from the WRF model at an altitude of 6 km, alongside the LH retrieved by the CNNH method, FCNH method, and VPH algorithm. When condensation or deposition is the main phase transition process in the precipitating clouds, the precipitation rate lapse rate is positive. At the lateral boundary of the precipitation system, when hydrometeors are facing the unsaturated air environment, they tend to evaporate or sublimate, and the precipitation rate lapse rate is negative [55]. At 6 km altitude, the spatial patterns of LH_{CNNH}, LH_{FCNH}, and LH_{VPH} captured the main spatial pattern of LH_{WRF}, with spatial correlation coefficients of 0.90, 0.79, and 0.74, respectively. At altitudes of 4, 5, 7, 8, and 9 km, the spatial correlation coefficients between LH_{CNNH} and LH_{WRF} are 0.88, 0.89, 0.90, 0.90, and 0.89, significantly higher than the spatial correlation coefficients between $\text{LH}_{\text{FCNH}}/\text{LH}_{\text{WRF}}$ and $\text{LH}_{\text{VPH}}/\text{LH}_{\text{WRF}}$ ($\text{LH}_{\text{FCNH}}/\text{LH}_{\text{WRF}}$ 0.67, 0.73, 0.77, 0.72, and 0.72; $\text{LH}_{\text{VPH}}/\text{LH}_{\text{WRF}}$ 0.58, 0.61, 0.73, 0.67, and 0.71; associated plots not shown).

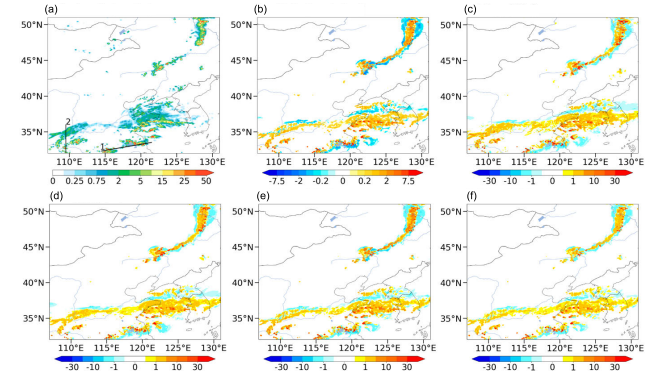

Fig. 3. Precipitation event at UTC 12:30 on August 27, 2017. (a) WRF simulated surface precipitation rate (mm/h). (b) $-dRr/dz$ (mm/h/km) at 6 km altitude. (c) WRF simulated LH at 6 km altitude (K/h). (d) LH retrieved by the CNNH method at 6 km altitude (K/h). (e) LH retrieved by the FCNH method at 6 km altitude (K/h). (f) LH retrieved by the VPH algorithm at 6 km altitude (K/h).

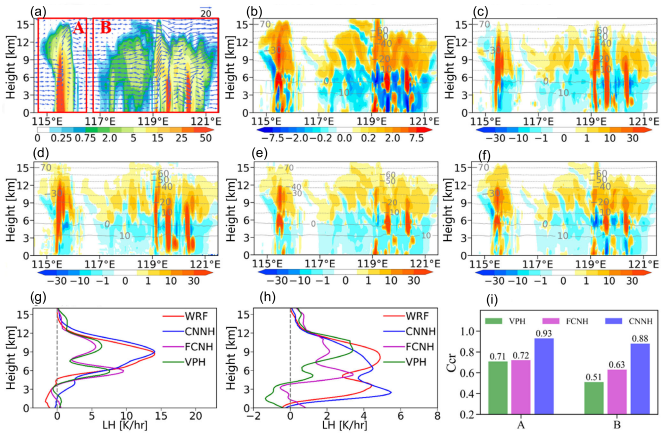

Fig. 4. Vertical cross sections along line 1 in Fig. 3(a) of (a) precipitation rate (mm/h). (b) $-dRr/dz$ (mm/h/km). (c) Simulated LH by WRF (K/h). (d) LH retrieved by the CNNH method (K/h). (e) LH retrieved by the FCNH method (K/h). (f) LH retrieved by the VPH algorithm. (g) Mean vertical profiles of LH retrieved by the four methods for System A. (h) Mean vertical profiles of LH retrieved by the four methods for System B. (i) Histograms of Ccr between LH_{CNNH}, LH_{FCNH}, and LH_{VPH} against LH_{WRF} for systems A and B.

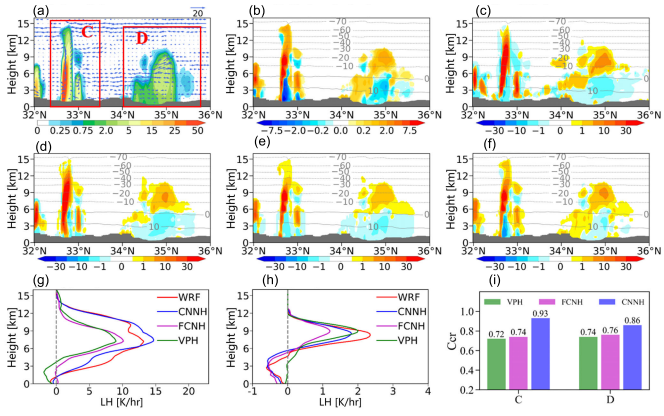

Fig. 5. Vertical cross sections along line 2 in Fig. 3(a) of (a) precipitation rate(mm/h). (b) $-dRr/dz$ (mm/h/km). (c) Simulated LH by WRF (K/h). (d) LH retrieved by the CNNH method (K/h). (e) LH retrieved by the FCNH method (K/h). (f) LH retrieved by the VPH algorithm. (g) Mean vertical profiles of LH retrieved by the four methods for System A. (h) Mean vertical profiles of LH retrieved by the four methods for System B. (i) Histograms of Ccr between LH_{CNNH}, LH_{FCNH}, and LH_{VPH} against LH_{WRF} for systems A and B.

Fig. 4 depicts the vertical structure of precipitation and LH along the line 1 in Fig. 3. Within Precipitation System A,

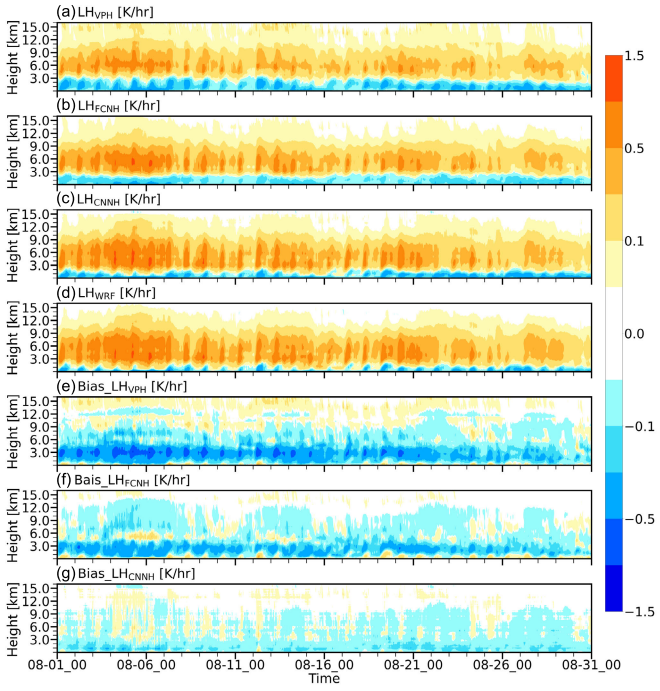

Fig. 6. Time-height cross sections of LH and associated biases from August 1 to 31, 2017. (a) LH retrieved by the VPH algorithm. (b) LH retrieved by the FCNH algorithm. (c) LH retrieved by the CNNH method. (d) LH simulated by the WRF model. (e) Bias of the VPH algorithm retrieval. (f) Bias of the FCNH algorithm retrieval. (g) Bias of LH for the CNNH algorithm retrieval.

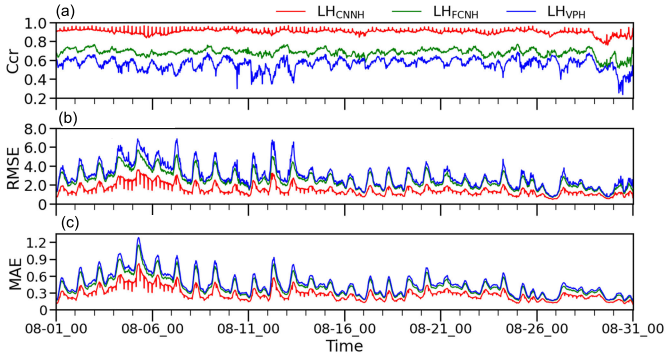

Fig. 7. Statistical indicators of LH retrieval in the study area from August 1 to 31, 2017: time series of (a) Ccr, (b) RMSE, and (c) MAE are between LH_{CNNH} (red), LH_{FCNH} (green), LH_{VPH} (blue) against LH_{WRF}, respectively.

there is a distinct deep convective core indicated by strong updraft velocity associated with precipitation top height of 15 km and surface precipitation rates exceeding 30 mm/h centered at ~115.2°E. In this area, the vertical distribution and the intensity of LH_{CNNH} closely match those of LH_{WRF}. Both show strong positive LH extending throughout the entire column at the left side of the convective core. Meanwhile, the WRF simulated flow field shows that the eastern part of system A is the outflow area of the vertical updraft in the convective core. Both LH_{CNNH} and LH_{VPH} show positive heating above the freezing layer and negative cooling beneath it [Fig. 4(c) and (d)], indicating a classical top-heavy stratiform LH pattern. For the other two algorithms, the LH_{FCNH} and LH_{VPH} show more departures from LH_{WRF} in System A [Fig. 4(c), (e), and (f)]. For instance, they both show cooling near the surface in the convection core area and some mixed

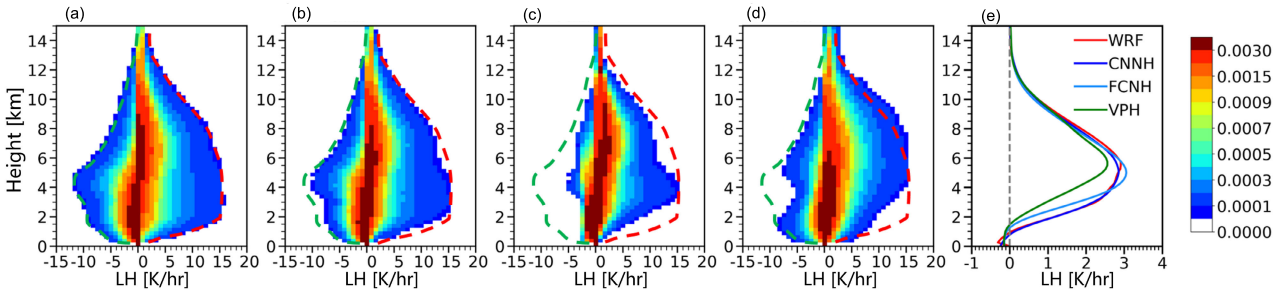

Fig. 8. (a)–(d) CFADs of WRF-retrieved LH, CNNH-retrieved LH, FCNH-retrieved LH, and VPH-retrieved LH. (e) Comparison of average vertical profiles of LH during August 1–31, 2017, in the study area. Overlapped red and green curves are the lateral boundaries of the WRF CFAD used as reference lines to compare with the other three CFADs.

in positive heating in the lower layer of the out-flow area. The mean vertical profiles [Fig. 4(g)] reveal that LH_{CNNH} (blue curve) and LH_{WRF} (red curve) all show one single heating peak of ∼14 K/h at the same altitude of ∼9 km, whereas LH_{FCNH} and LH_{VPH} showed two heating peaks at approximately 10.5 and 5.5 km with much lower peak heating intensities than LH_{WRF}.

In the precipitation system B, LH_{CNNH} also agrees better with LH_{WRF}. The CNNH method significantly reduced the discontinuity of some heating or cooling zones at medium and low altitudes because the CNNH algorithm designs additional loss penalties, so some negative Γ values in Fig. 4(b) still correspond to LH heating, which is also due to the fact that CNNH takes into account horizontal and vertical neighborhood information, which will be discussed in detail later.

Quantitatively, the correlation coefficients of the vertical distribution of LH_{CNNH} against LH_{WRF} are 0.93 and 0.88 for precipitation systems A and B, respectively. These values are all higher than those of LH_{VPH} and LH_{FCNH} [Fig. 4(i)].

Fig. 5 presents vertical cross sections of LH and precipitation along line 2 depicted in Fig. 3(a). In precipitation system C, LH_{CNNH}, LH_{FCNH}, and LH_{VPH} all capture the major characteristics of LH_{WRF}, reaching the maximum LH at similar altitudes (around 7 km). However, LH_{VPH} exhibits strong cooling below 4 km in the convective center, resulting in a positive-to-negative transition in the average vertical profile of LH below about 4 km, which differs significantly from LH_{WRF}. Precipitation system D represents a typical stratiform precipitation system, where LH_{CNNH}, LH_{FCNH}, and LH_{WRF} all exhibit positive LH above and negative LH below the freezing level. Nonetheless, LH_{VPH} shows more heating LH below the freezing level, indicating a noticeable difference from the distribution of LH_{WRF}. From the average vertical profiles [Fig. 5(g) and (h)] and spatial correlation coefficients [Fig. 5(i)], it can be observed that among the three retrieval methods, the CNNH method achieves the highest retrieving accuracy of LH compared to the LH_{WRF} as ground truth.

B. Statistical Study

In order to evaluate the capability of the CNNH method to retrieve the time evolution of LH 3-D structure, statistical analysis was conducted on the one-month LH retrieval from the CNNH algorithm, covering the period from August 1 to August 31, 2017. A comparison was made with the true values of LH simulated by the WRF model, as well as the LH retrieval results obtained using the FCNH method and VPH algorithm.

The temporal evolution of vertical structures of LH_{WRF} retrieved by three algorithms (LH_{CNNH}, LH_{FCNH}, and LH_{VPH}) are displayed in Fig. 6. At regional averages, LH_{WRF} [Fig. 6(d)] primarily exhibits positive heating with its peak intensity occurring within the 3–8 km altitude while showing only weak cooling effects below 2 km. The LH_{VPH} [Fig. 6(a)] shows a much thicker cooling layer near the surface, demonstrating substantial overestimation of cooling under 3 km and notably weaker positive heating between 3 and 8 km relative to LH_{WRF}, thus leading to pronounced negative biases [Fig. 6(e)] in LH_{VPH}, particularly within the near-surface layer. The FCNH method [Fig. 6(b)], leveraging the superior non-linear mapping capabilities of neural networks, improves upon the underestimate of LH present in the VPH algorithm to some extent; however, it overestimates the heating effect in the mixing layer (about 6 km). By contrast, the CNNH method [Fig. 6(c)], building upon the FCNH approach, takes into account the influence of hydrometeor horizontal and vertical displacement as well as vertical profile structure on LH retrieval from precipitation. CNNH effectively addresses the issue of overestimating cooling near the surface and heating in the mixing layer found in the FCNH method. Consequently, the mean vertical distribution of LH_{CNNH} aligns closely with that of LH_{WRF} and shows the smallest bias [Fig. 6(g)]. Based on the one-month simulated data, the overall average biases between LH_{CNNH}, LH_{FCNH}, LH_{VPH}, and LH_{WRF} are −0.02, −0.04, and −0.09 K/h, respectively.

The time series of the MAE, RMSE, and spatial correlation coefficient (Ccr) for LH_{CNNH}, LH_{FCNH}, LH_{VPH}, and LH_{WRF} are shown in Fig. 7. The MAE of LH_{CNNH}, LH_{FCNH}, and LH_VPH are 0.2, 0.4, and 0.5 K/h, respectively, while their RMSEs are 1.46, 2.50, and 2.73 K/h, respectively. The spatial correlation coefficients (Ccr) average out to 0.90, 0.68, and 0.56 for LH_{CNNH}, LH_{FCNH}, and LH_{VPH} correspondingly.

To reveal the probability distribution of LH retrievals, the contoured frequency by altitude diagrams (CFADs) of the four LHs are shown in Fig. 8. As the ground truth, the LH_{WRF} is broadly distributed across nearly all vertical levels. In contrast, LH_{VPH} shows distinct differences from LH_{WRF} in terms of its maximum probability distribution. The probability distribution of LH_{VPH} below 5 km is too concentrated in the region around

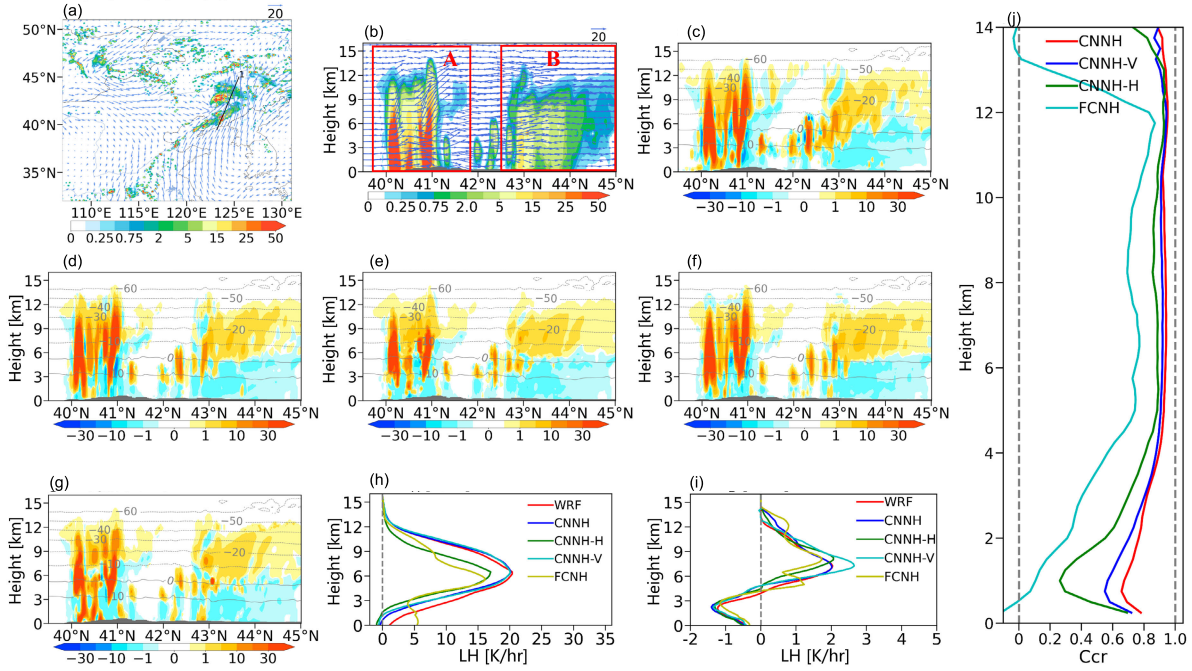

Fig. 9. Precipitation case at UTC 06:00 on August 3, 2017. (a) Surface precipitation rate (mm/h); vertical cross sections along the line 1. (b) Precipitation rate (mm/h). (c) WRF-simulated LH (K/h). (d) LH retrieved by the CNNH method (K/h). (e) LH retrieved by the CNNH-H method (K/h). (f) LH retrieved by the CNNH-V algorithm. (g) LH retrieved by the FCNH algorithm. (h) Average vertical profiles of LH for System A using the four different retrieval methods. (i) Average vertical profiles of LH for System B using the four different retrieval methods. (j) Ccr between the LH retrieved by four methods and WRF-modeled LH.

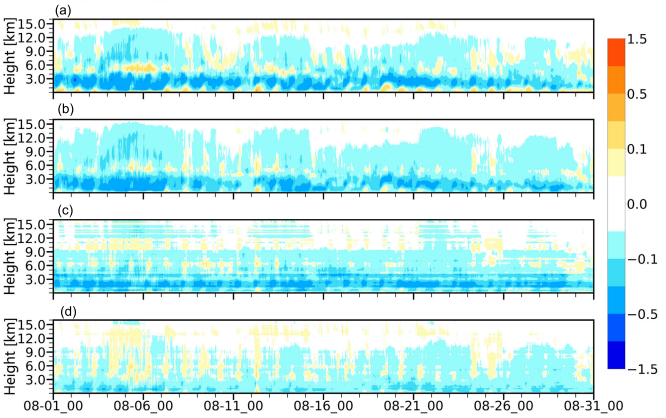

Fig. 10. Time-height cross sections of LH biases during August 1–31, 2017. (a) Bias of LH for the FCNH algorithm. (b) Bias of LH for the CNNH-H method. (c) Bias of LH for the CNNH-V. (d) Bias of LH for the CNNH method.

the 0 value. Although LH_{FCNH} aligns better with the major characteristics of the maximum probability LH distribution of LH_{WRF}, the FCNH method appears not to have learned the marginal information due to the uneven distribution of LH data. At all altitudes, the probability distribution range of LH_{FCNH} is much smaller than that of LH_{WRF}. Meanwhile, LH_{CNNH}'s CFAD makes up for the above shortcomings of LH_{VPH} and LH_{FCNH}, and its CFAD is almost identical to LH_{WRF}, with only a little missing in the most marginal area; perhaps this can be improved later by increasing the number of learned samples and increasing the representative performance of extreme events in the learning samples.

From Fig. 8(e), the monthly mean vertical profiles of LH_{CNNH} closely resemble that of LH_{WRF}, with comparable heating peaks around 5 km (~3 K/h). The VPH algorithm underestimates the heating below 7 km, whereas the FCNH method overestimates the peak LH in the mixing layer and underestimates it below 3.5 km. Overall, the CNNH method outperforms both FCNH and VPH algorithms in capturing the distribution of WRF-simulated LH with greater fidelity.

C. Impacts of Horizontal Neighborhood Information and Vertical Profile Structure

In order to reveal why the 3-D-CNN method is so effective in improving the accuracy of retrieved LH, we designed two sensitivity experiments to understand the importance of adding horizontal and vertical neighborhood information. We designed a CNNH-H method, which only incorporates horizontal neighborhood information, and a CNNH-V method, which only incorporates vertical profile information. Their retrieval performances are compared with that of the full CNNH method, which combines both the horizontal neighborhood information and the vertical profile structure.

First, we use a case study to compare the retrieving performances of the above three methods in detail. This case occurred at UTC 06:00 on August 3, 2017, in a typical mesoscale frontal precipitation system in the Liaoning and Jilin regions of China, where cold air from the northwest met warm and humid air masses from the Bohai Sea in the south, forming a rain belt trending southwest to northeast of about 1500 km [Fig. 9(a)]. The vertical cross section of WRF simulations shows that there is a strong LH release

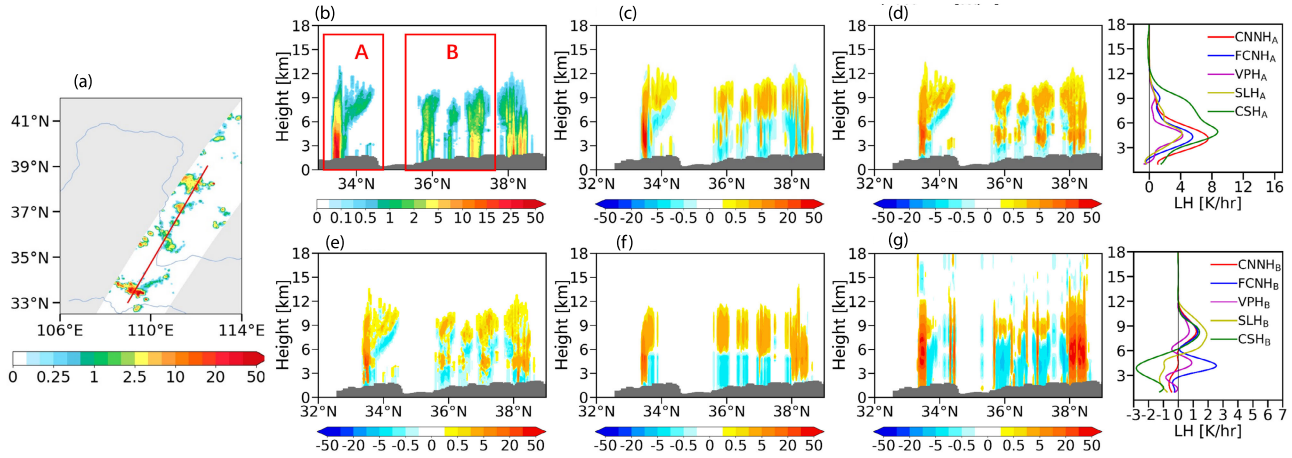

Fig. 11. Case of precipitation observed by GPM DPR at UTC 10:53:00 on July 14, 2017. (a) Horizontal distribution of surface precipitation rates; vertical cross sections along the straight line of (b) precipitation rate. (c) LH retrieved by the CNNH method. (d) LH retrieved by FCNH method. (e) LH retrieved by the VPH method. (f) LH retrieved by SLH method. (g) LH retrieved by CSH method. The mean profiles of LH associated with selected systems A and B are shown in the right column.

on the side of the rain band near the warm air mass, and significant LH absorption and cooling at the low layers on the side of the rain band near the northwest cold air mass, and the interface between the two forms an obvious inclined front structure [Fig. 9(c)]. The CNNH algorithm can retrieve the above LH vertical structure well, and the overall correlation coefficient reaches 0.90 [Fig. 9(d)]. When only the horizontal neighborhood information is considered in the retrieval [i.e., CNNH-H, Fig. 9(e)], in the south side of the front system (e.g., 40°–41°N), the retrieved convection heating is weak, the vertical extension of strong heating is lower, and the intensity of the updraft condensation heating above the front is also low. When considering the vertical structure information [i.e., CNNH-V, Fig. 9(f)], the convective heating is significantly strengthened, and from the average profile, the LH_{CNNH-H} is systematically lower by 2–3 K/h in the convective heating region [Fig. 9(h)], while the LH_{CNNH-V} and LH_{CNNH} are very close to the modeling true value LH_{WRF} above 4 km, while below 4 km, there is still an underestimation of 1–2 K/h. In the stratiform precipitation region to the north of the front, all retrievals show a significant vertical distribution of LH of positive above and negative cooling below the freezing level, and LH_{CNNH} is in good agreement with the true value of the model LH_{WRF}, while LH_{CNNH-H} significantly underestimates the heating in the mixing layer and LH_{CNNH-V} significantly overestimates the heating in the upper layer. From the correlation coefficient curve [Fig. 9(j)], it can be seen that the retrieved LH of CNNH, CNNH-V, and CNNH-H has a high correlation coefficient with the WRF-modeled LH, which is greater than 0.8 overall. Comparing several models, the correlation coefficients $Ccr_{CNNH} > Ccr_{CNNH-V} > Ccr_{CNNH-H} > Ccr_{FCNH}$, indicate that both vertical profile structure information and horizontal neighborhood information can improve the accuracy of LH retrieval, and the vertical profile information is more effective than horizontal neighborhood information.

Second, we compared the temporal evolution process of LH_{CNNH-H} and LH_{CNNH-V}. Fig. 10 presents the time-height cross sections of LH biases over a continuous one-month period. The FCNH method solely relies on learning the nonlinear mapping between input information within the signal pixel grid and LH for retrieval purposes. Observations indicate that: 1) the inclusion of either horizontal neighborhood information or vertical profile structure information can suppress the underestimation of LH below 4 km and correct overestimations in the mixing layer; 2) vertical profile structure information proves more effective than horizontal neighborhood information in mitigating the underestimation of LH near the surface; and 3) combining both horizontal neighborhood information and vertical profile structure information further enhances the performance of LH retrieval.

In addition, the environmental temperature can provide the location of the freezing level and indicate the phase state of hydrometeors, playing a significant role in LH retrieval. When the environmental temperature was removed from the inputs, the performance of the CNNH model decreased significantly. The MAE and RMSE between the retrieved LH and the WRF-modeled LH increased from 0.20 and 1.46 K/h to 0.25 and 1.76 K/h, respectively. The Ccr decreased from 0.90 to 0.83.

V. Retrieving LH Using GPM DPR Measurements

The CNNH has been developed and evaluated using WRF model simulation data; now, we apply it to real satellite observation data. Since LH lacks direct observational measurements, the CNNH method is applied to precipitation profiles derived from GPM DPR observations, and its LH retrieval results are compared against those from the FCNH algorithm, VPH algorithm, and the GPM operational SLH, CSH algorithms. It should be emphasized that there is some significant topography in these cross sections. CSH LH should be used cautiously around these regions as it currently does not have LUTs for terrain, whereas SLH does. The sparsity of CSH data in the terrain impacts its cross sections as spatial interpolation was used to create the cross sections.

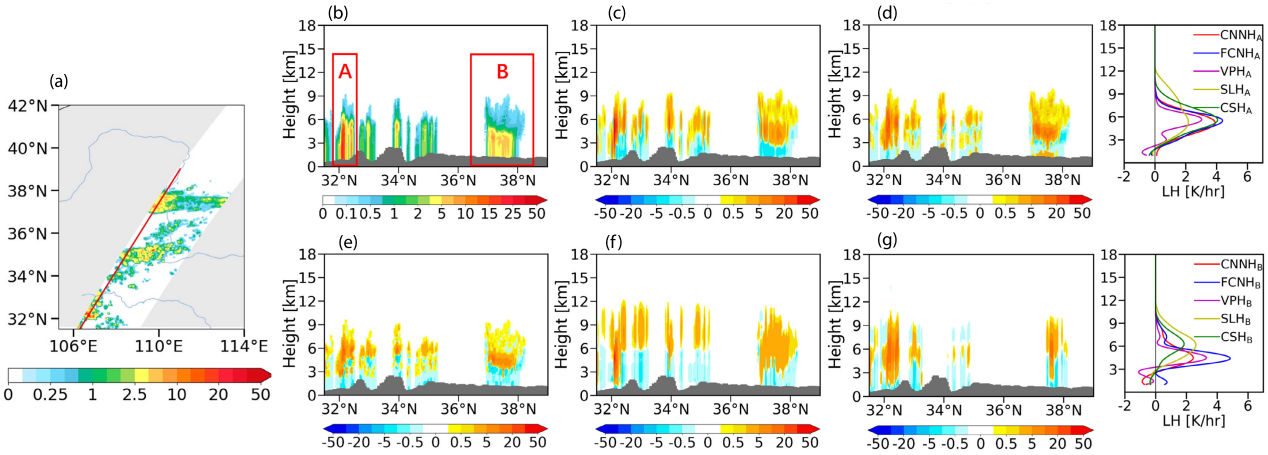

Fig. 12. Case of precipitation observed by the GPM DPR at UTC 21:39:00 on August 28, 2017. (a) Horizontal distribution of surface rain rates; vertical cross sections along the straight line of (b) precipitation rate. (c) LH retrieved by the CNNH method. (d) LH retrieved by the FCNH method. (e) LH retrieved by the VPH method. (f) LH retrieved by SLH method. (g) LH retrieved by CSH method. The mean profiles of LH associated with selected systems A and B are shown in the right column.

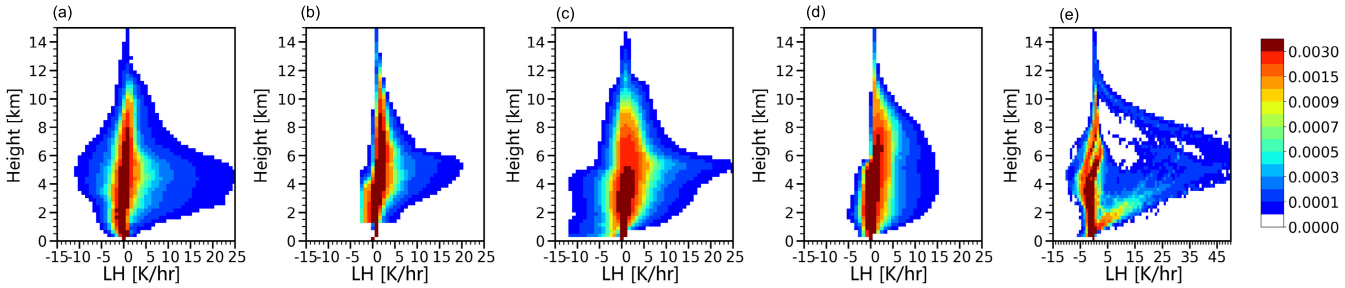

Fig. 13. CFADs during five months (May–September 2017) within the study area of (a) LH retrieved by the CNNH method. (b) LH retrieved by the FCNH method. (c) LH retrieved by the VPH algorithm. (d) LH retrieved by the SLH algorithm. (e) LH retrieved by the CSH algorithm.

Fig. 11 displays a precipitation case observed by GPM DPR at UTC 10:53:00 on July 14, 2017. In region A, a mesoscale convective system (MCS) with a strong convective core was observed around 33.5°N, where surface precipitation rates exceed 25 mm/h. On the north side, precipitation significantly weakens, with surface precipitation rates below 2 mm/h, and a virga is observed above 6 km. The retrieved LH from the SLH, CSH, CNNH, VPH, and FCNH methods all show positive heating near 33.5°N, while in the stratiform precipitation area on the right side, all retrievals show positive LH above and negative LH below. It is worth noting that the CNNH, FCNH, and VPH algorithms successfully retrieve the LH associated with the virga, whereas the SLH and CSH methods fail to capture this portion of the LH, possibly due to the absence of such precipitation events in their LUTs. The four algorithms yield similar average vertical profiles, with the maximum values of LH achieved at similar heights of 4–5 km. In terms of the amplitude of the peak heating, the CSH algorithm shows the largest heating of ∼9 K/h, followed by our CNN algorithm of ∼8 K/h, while the VPH and SLH provide the smallest estimation of ∼4 K/h. Additionally, SLH uses surface precipitation rates from the GPM DPR, while CSH uses surface precipitation rates from the GPM combined algorithm. Those differences in surface precipitation rates could explain some of the differences in magnitude between CSH and SLH and the other methods to some extent.

In Region B, there are several isolated weak convective cells with surface precipitation rates of 0.5–5 mm/h. LH_{CNNH} shows stratiform-dominant vertical distribution with heating aloft and cooling beneath 6 km. However, there are still some areas showing positive heating at layers 3–6 km. It was remarkable that LH_{SLH} showed a completely stratiform type with a clear dividing line of positive and negative LH at about 6 km. The LH_{FCNH} and LH_{VPH} show more positive heating at the lower layer (3–6 km) compared to those of LH_{CNNH}. The positive–negative interface is also more variable in CSH as well as CNNH, FCNH, and VPH versus SLH.

Fig. 12 depicts a well-organized MCS observed by GPM DPR at UTC 21:39:00 on August 28, 2017. In region A, with a strong convection core, LH_{CNNH}, LH_{CSH}, and LH_{SLH} show convective heating from the surface to the upper altitude, but the positive LH estimated by CSH and SLH extends to a higher height than LH_{CNNH}. In contrast, LH_{VPH} and LH_{FCNH} show some negative LH near the surface, which is most likely a retrieving error. In addition, LH_{VPH} and LH_{FCNH} also likely overestimate LH heating around 4–5 km. In region B, with relatively uniform rain, LH_{CNNH}, LH_{VPH}, LH_{FCNH}, and LH_{SLH} all show clear upper heating and low cooling structure divided at ∼3 km. For the CSH algorithm, retrievals over high terrain are set to missing, which will cause the retrieved area to appear reduced in regions with heights both above and below the threshold.

CFADs of five months (May–September 2017) of retrieved LH from the five algorithms (Fig. 13) show that the maximum probability distributions from the CNNH, FCNH, VPH, and SLH methods are generally similar, while the CSH CFAD has some noticeable differences with a more bimodal distribution at low levels and broader positive distribution at middle levels. This may be due in part to CSH having fewer samples from more missing values over higher terrain. CFADs of retrieved LH for CNNH, VPH, and especially CSH extend over a broader range than those from FCNH and SLH, which are relatively narrow.

Regarding the negative part of the CFADs (the left side of Fig. 13), CNNH, VPH, and CSH all display wide distributions, yet VPH tends to infer more cooling below 4 km. This suggests that GPM DPR observes numerous cases with negative precipitation rate gradients (i.e., $\Gamma = -dRr/dz$) near the surface, partly resulting from evaporation and partly from non-phase changing processes such as horizontal advection or breakup of raindrops [55]. VPH linearly maps all negative Γ to negative LH, leading to an overestimation of cooling, whereas CNNH accounts for the impact of hydrometeor horizontal displacement on precipitation LH and uses a CNN to learn the nonlinear mapping between Γ and LH, effectively correcting this overestimation. The narrow distribution of retrieved LH_{FCNH} at various altitudes may be attributed to its inability to capture the edge information. The SLH's narrow LH distribution above 2 km implies a weak association between negative Γ and cooling in the SLH algorithm. This is most likely due to the 5-min averaging of SLH in the SLH LUTs.

For the positive part of the CFADs for retrieved LH (the right side of Fig. 13), CSH, CNNH, FCNH, and VPH algorithms show relatively consistent distributions, except that FCNH misses the edge information (low-probability LH). The SLH algorithm does not depict positive LH exceeding 15 K/h, indicating that for given near-surface rainfall rates, cloud-top heights, and precipitation types in GPM DPR observations, SLH's LUT does not contain such high LH values. Again, this is likely from the 5-min averag in SLH. Nevertheless, extremely large Γ values must exist in mid-level atmospheric (e.g., 3–6 km) precipitation profiles, as inferred by the fact that CSH, CNNH, VPH, and FCNH methods all associate this with high LH release rates.

VI. Conclusion

This article proposes a new CNNH algorithm for satellite remote sensing to retrieve latent heating rates from precipitation profiles. The CNNH algorithm uses spaceborne microwave radar measured vertical gradient of precipitation rate ($\Gamma = -dR/dZ$) and air temperature at a given altitude as the main inputs to estimate the heating rate released at that point with three innovative features.

First, different from the previous algorithm, which only considers the local precipitation information, this CNNH algorithm also combines the precipitation and atmospheric state information at similar levels in the horizontal neighborhood and vertical directions, thus formulating a 3-D CNN structure. Second, in order to reduce the additional error caused by misjudging the release and absorption of latent heat, a special punishment LH-structure loss function is designed in addition to the conventional RMSE loss function. Third, an ADE algorithm was used to find the best settings of the CNNH network hyperparameter to improve the model performance.

Evaluations based on state-of-the-art cloud numerical modeling results showed that the CNNH method is significantly better than the two selected physical-based and AI-based LH algorithms (named VPH and FCNH) in terms of MAE, RMSE, BAIS, and Ccr. The reason for such improvement can be explained in three aspects.

1) The VPH and FCNH algorithms regard the decrease of rain rate toward the surface (i.e., negative $\Gamma = -dRr/dz$) as an evaporation process, ignoring the possible non-phase changing processes such as raindrop breakup, thus resulting in significant overestimation of cooling in low layers near the surface. The CNNH method, from learning the cloud numerical modeling truth of latent heat and rain rate, has a self-adaptive function to relieve such overestimation through the designed LH-structure loss function while taking advantage of the combined horizontal and vertical structural information in the network design.
2) The FCNH method missed the LH releasing events with small occurring probability mainly due to sample imbalance between different types of precipitation. The CNNH method integrates the horizontal neighborhood information and vertical structure of input data as the combined input into the network, thus balancing the sample distribution to a certain extent, and introduces more physical information. Therefore, CNNH results in a more consistent probability distribution of LH with cloud modeling results.
3) The comprehensive design of the CNNH method enables it to have stronger complex nonlinear mapping capabilities and improves the retrieval accuracy of the mixing layer, which contains complex and diverse phase change processes, including melting, freezing, deposition, and sublimation.

Further investigations show that the horizontal neighboring information can improve the performance of retrieving LH, particularly in stratiform precipitation. However, vertical profile structure is significantly more important in LH retrieval for both convective and stratiform precipitation. This may be because the local LH in the stratiform precipitation system has stronger connections with the neighboring horizontal area. And in both convective and stratiform precipitation, the local phase changing processes are highly related to updraft velocity, which makes strong impacts on the vertical structure of precipitation.

The retrieving algorithm was tested by using the GPM-DPR satellite observation data. The CNNH method retrieved LH, and the four other published LH products show relatively consistent vertical structure. However, these algorithms still have significant differences in the heating of vigor, the near-surface heating of convective precipitation, the heating in the

cooling layer of stratiform precipitation, and the heating peak amplitude, indicating that there are considerable uncertainties in multiple LH satellite remote sensing products.

This study is the first attempt to use CNN machine learning method to deal with satellite remote sensing latent heating. It not only deepens the understanding of using the AI method in solving retrieval problem in the field of atmospheric remote sensing but also provides an important basis for constructing a more efficient and accurate retrieval model.

ACKNOWLEDGMENT

The authors deeply appreciate the constructive comments of the two anonymous reviewers. They sincerely thank NASA for providing the data that made this research possible; their commitment to open-access data has greatly supported their work.

CREDIT AUTHORSHIP CONTRIBUTION STATEMENT

Hongwei Zhao: Conceptualization, data curation, formal analysis, investigation, methodology, software, validation, visualization, and writing—original draft. Shuping Yang: Data curation, software. Qiong Wu: Investigation and data curation. Lin Chen: Funding acquisition, investigation, and supervision. Peng Zhang: Methodology, project administration, and supervision. Rui Li: Conceptualization, formal analysis, funding acquisition, investigation, methodology, writing—original draft, writing—review and editing, supervision, and project administration.

DATA AVAILABILITY STATEMENT

The GPM standard products 2ADPR, 2ADPR ENV, 2HSLH, and 2HCSH used in this study were downloaded from https://storm.pps.eosdis.nasa.gov.

The datasets that support the described results and allow other readers to assess our conclusions are provided at https://doi.org/10.5281/zenodo.12531329 [56].

REFERENCES

[1] X. Luo, J. Fei, X. Huang, J. Ding, and Z. Ma, "Relative roles of dry intrusion, latent heat and instabilities in the Mei-yu rainband life cycle: A case study," *Atmos. Res.*, vol. 214, pp. 10–20, Dec. 2018, doi: 10.1016/j.atmosres.2018.07.007.

[2] E. L. Nelson and T. S. L'Ecuyer, "Global character of latent heat release in oceanic warm rain systems," *J. Geophys. Res., Atmos.*, vol. 123, no. 10, pp. 4797–4817, May 2018, doi: 10.1002/2017jd027844.

[3] C. Kummerow et al., "The status of the tropical rainfall measuring mission (TRMM) after two years in orbit," *J. Appl. Meteorol.*, vol. 39, no. 12, pp. 1965–1982, 2000.

[4] W.-K. Tao et al., "Retrieval of latent heating from TRMM measurements," *Bull. Amer. Meteorol. Soc.*, vol. 87, no. 11, pp. 1555–1572, Nov. 2006.

[5] Y. Liu, J. Huang, T. Wang, J. Li, H. Yan, and Y. He, "Aerosol-cloud interactions over the Tibetan Plateau: An overview," *Earth-Sci. Rev.*, vol. 234, Nov. 2022, Art. no. 104216.

[6] C. Zhao et al., "Observational evidence and mechanisms of aerosol effects on precipitation," *Sci. Bull.*, vol. 69, no. 10, pp. 1569–1580, May 2024.

[7] Y. Li and Y. Gal, "Dropout inference in Bayesian neural networks with alpha-divergences," 2017, *arXiv:1703.02914*.

[8] Y. Wu and Y. Peng, "Investigation of aerosol effects on a deep convection case in southeast China with budget analysis of hydrometeor mass and latent heat," *Atmos. Res.*, vol. 277, Oct. 2022, Art. no. 106275.

[9] W.-K. Tao et al., "TRMM latent heating retrieval: Applications and comparisons with field campaigns and large-scale analyses," *Meteorol. Monographs*, vol. 56, pp. 2.1–2.34, Apr. 2016, doi: 10.1175/amsmonographs-d-15-0013.1.

[10] S. Hagos et al., "Estimates of tropical diabatic heating profiles: Commonalities and uncertainties," *J. Climate*, vol. 23, no. 3, pp. 542–558, Feb. 2010.

[11] W.-K. Tao, S. Lang, J. Simpson, and R. Adler, "Retrieval algorithms for estimating the vertical profiles of latent heat release: Their applications for TRMM TRMM," *J. Meteorol. Soc. Jpn. II*, vol. 71, no. 6, pp. 685–700, 1993, doi: 10.2151/jmsj1965.71.6_685.

[12] W.-K. Tao et al., "Vertical profiles of latent heat release and their retrieval for TOGA COARE convective systems using a cloud resolving model, SSM/I, and ship-borne radar data," *J. Meteorol. Soc. Jpn. II*, vol. 78, no. 4, pp. 333–355, 2000, doi: 10.2151/jmsj1965.78.4_333.

[13] S. Shige, Y. N. Takayabu, W.-K. Tao, and D. E. Johnson, "Spectral retrieval of latent heating profiles from TRMM PR data. Part I: Development of a model-based algorithm," *J. Appl. Meteorol.*, vol. 43, no. 8, pp. 1095–1113, 2004, doi: 10.1175/1520-0450(2004)043<1095:SROLHP>2.0.CO;2.

[14] S. Shige, Y. N. Takayabu, W.-K. Tao, and C.-L. Shie, "Spectral retrieval of latent heating profiles from TRMM PR data. Part II: Algorithm improvement and heating estimates over tropical ocean regions," *J. Appl. Meteorol. Climatol.*, vol. 46, no. 7, pp. 1098–1124, Jul. 2007, doi: 10.1175/jam2510.1.

[15] S. Shige, Y. N. Takayabu, and W.-K. Tao, "Spectral retrieval of latent heating profiles from TRMM PR data. Part III: Estimating apparent moisture sink profiles over tropical oceans," *J. Appl. Meteorol. Climatol.*, vol. 47, no. 2, pp. 620–640, Feb. 2008, doi: 10.1175/2007jamc1738.1.

[16] M. Grecu, W. S. Olson, C.-L. Shie, T. S. L'Ecuyer, and W.-K. Tao, "Combining satellite microwave radiometer and radar observations to estimate atmospheric heating profiles," *J. Climate*, vol. 22, no. 23, pp. 6356–6376, Dec. 2009, doi: 10.1175/2009jcli3020.1.

[17] W.-K. Tao, S. Lang, X. Zeng, S. Shige, and Y. Takayabu, "Relating convective and stratiform rain to latent heating," *J. Climate*, vol. 23, no. 7, pp. 1874–1893, Apr. 2010, doi: 10.1175/2009jcli3278.1.

[18] S. E. Lang and W.-K. Tao, "The next-generation Goddard convective–stratiform heating algorithm: New tropical and warm-season retrievals for GPM," *J. Climate*, vol. 31, no. 15, pp. 5997–6026, Aug. 2018, doi: 10.1175/jcli-d-17-0224.1.

[19] W.-K. Tao, T. Iguchi, and S. Lang, "Expanding the Goddard CSH algorithm for GPM: New extratropical retrievals," *J. Appl. Meteorol. Climatol.*, vol. 58, no. 5, pp. 921–946, May 2019.

[20] W.-K. Tao, S. Lang, T. Iguchi, and Y. Song, "Goddard latent heating retrieval algorithm for TRMM and GPM TRMM/GPM Goddard," *J. Meteorol. Soc. Jpn. II*, vol. 100, no. 2, pp. 293–320, 2022, doi: 10.2151/jmsj.2022-015.

[21] S. Shige et al., "Spectral retrieval of latent heating profiles from TRMM PR data. Part IV: Comparisons of lookup tables from two-and three-dimensional cloud-resolving model simulations," *J. Climate*, vol. 22, no. 20, pp. 5577–5594, 2009, doi: 10.1175/2009JCLI2919.1.

[22] S. Shige, S. Kida, H. Ashiwake, T. Kubota, and K. Aonashi, "Improvement of TMI rain retrievals in mountainous areas," *J. Appl. Meteorol. Climatol.*, vol. 52, no. 1, pp. 242–254, Jan. 2013, doi: 10.1175/jamc-d-12-074.1.

[23] W.-K. Tao, J. Simpson, S. Lang, M. McCumber, R. Adler, and R. Penc, "An algorithm to estimate the heating budget from vertical hydrometeor profiles," *J. Appl. Meteorol.*, vol. 29, no. 12, pp. 1232–1244, Dec. 1990, doi: 10.1175/1520-0450(1990)029<1232:AATETH>2.0.CO;2.

[24] S. Yang and E. A. Smith, "Moisture budget analysis of TOGA COARE area using SSM/I-retrieved latent heating and large-scale Q_2 estimates," *J. Atmos. Ocean. Technol.*, vol. 16, no. 6, pp. 633–655, 1999, doi: 10.1175/1520-0426(1999)016<0633:MBAOTC>2.0.CO;2.

[25] S. Yang and E. A. Smith, "Four-dimensional structure of monthly latent heating derived from SSM/ISatellite measurements," *J. Climate*, vol. 12, no. 4, pp. 1016–1037, 1999, doi: 10.1175/1520-0442(1999)012<1016:FDSOML>2.0.CO;2.

[26] S. Yang and E. A. Smith, "Vertical structure and transient behavior of convective–stratiform heating in TOGA COARE from combined satellite–sounding analysis," *J. Appl. Meteorol.*, vol. 39, no. 9, pp. 1491–1513, Sep. 2000, doi: 10.1175/1520-0450(2000)039<1491:VSATBO>2.0.CO;2.

[27] S. Satoh, A. Noda, and T. Iguchi, "Retrieval of latent heating profiles from TRMM radar data," in *Proc. 30th Int. Conf. Radar Meteorol.*, vol. 6. Munich, Germany: American Meteorological Society, 2001, pp. 340–342.

[28] G. Liu and Y. Fu, "The characteristics of tropical precipitation profiles as inferred from satellite radar Measurements.," *J. Meteorol. Soc. Jpn. II*, vol. 79, no. 1, pp. 131–143, 2001, doi: 10.2151/jmsj.79.131.

[29] Y. Fu and G. Liu, "The variability of tropical precipitation profiles and its impact on microwave brightness temperatures as inferred from TRMM data," *J. Appl. Meteorol.*, vol. 40, no. 12, pp. 2130–2143, Dec. 2001, doi: 10.1175/1520-0450(2001)040<2130:TVOTPP>2.0.CO;2.

[30] R. Li, Q. Min, and Y. Fu, "1997/98 el Niño–Induced changes in rainfall vertical structure in the east Pacific," *J. Climate*, vol. 24, no. 24, pp. 6373–6391, Dec. 2011, doi: 10.1175/jcli-d-11-00002.1.

[31] Q. Min, R. Li, X. Wu, and Y. Fu, "Retrieving latent heating vertical structure from cloud and precipitation profiles—Part I: Warm rain processes," *J. Quant. Spectrosc. Radiat. Transf.*, vol. 122, pp. 31–46, Jun. 2013, doi: 10.1016/j.jqsrt.2012.11.030.

[32] R. Li, Q. Min, X. Wu, and Y. Fu, "Retrieving latent heating vertical structure from cloud and precipitation profiles—Part II: Deep convective and stratiform rain processes," *J. Quant. Spectrosc. Radiat. Transf.*, vol. 122, pp. 47–63, Jun. 2013, doi: 10.1016/j.jqsrt.2012.11.029.

[33] R. Li et al., "A simplified algorithm to estimate latent heating rate using vertical rainfall profiles over the Tibetan Plateau," *J. Geophys. Res., Atmos.*, vol. 124, no. 2, pp. 942–963, Jan. 2019, doi: 10.1029/2018jd029297.

[34] H. Zhao et al., "Satellite-based fully connected neural network heating (FCNH) algorithm for estimating latent heating rate inside storms," *J. Geophys. Res., Atmos.*, vol. 128, no. 19, Oct. 2023, Art. no. e2022JD038448.

[35] C. Zhao and T. J. Garrett, "Ground-based remote sensing of precipitation in the Arctic," *J. Geophys. Res., Atmos.*, vol. 113, no. D14, Jul. 2008, Art. no. D14204, doi: 10.1029/2007JD009222.

[36] M. Sadeghi, P. Nguyen, K. Hsu, and S. Sorooshian, "Improving near real-time precipitation estimation using a U-Net convolutional neural network and geographical information," *Environ. Model. Softw.*, vol. 134, Dec. 2020, Art. no. 104856.

[37] T. Tu, K. Ishida, A. Ercan, M. Kiyama, M. Amagasaki, and T. Zhao, "Hybrid precipitation downscaling over coastal watersheds in Japan using WRF and CNN," *J. Hydrol., Regional Stud.*, vol. 37, Oct. 2021, Art. no. 100921.

[38] D. Niu, L. Diao, L. Xu, Z. Zang, X. Chen, and S. Liang, "Precipitation forecast based on multi-channel ConvLSTM and 3D-CNN," in *Proc. Int. Conf. Unmanned Aircr. Syst. (ICUAS)*, Sep. 2020, pp. 367–371.

[39] F. King, G. Duffy, L. Milani, C. G. Fletcher, C. Pettersen, and K. Ebell, "DeepPrecip: A deep neural network for precipitation retrievals," *Atmos. Meas. Techn.*, vol. 15, no. 20, pp. 6035–6050, Oct. 2022.

[40] Y. Jing, L. Lin, X. Li, T. Li, and H. Shen, "An attention mechanism based convolutional network for satellite precipitation downscaling over China," *J. Hydrol.*, vol. 613, Oct. 2022, Art. no. 128388.

[41] J. Zhang and A. C. Sanderson, *Adaptive Differential Evolution*. Berlin, Germany: Springer, 2009, pp. 83–93.

[42] A. Y. Hou et al., "The global precipitation measurement mission," *Bull. Amer. Meteorol. Soc.*, vol. 95, no. 5, pp. 701–722, May 2014, doi: 10.1175/BAMS-D-13-00164.1.

[43] T. Iguchi and R. Meneghini, "GPM DPR precipitation profile L2A 1.5 hours 5 km V06," Goddard Earth Sci. Data Inf. Services Center (GES DISC), Greenbelt, MD, USA, Rep., 2017, doi: 10.5067/GPM/DPR/GPM/2A/06.

[44] J. G. Powers et al., "The weather research and forecasting model: Overview, system efforts, and future directions," *Bull. Amer. Meteorol. Soc.*, vol. 98, no. 8, pp. 1717–1737, Aug. 2017, doi: 10.1175/BAMS-D-15-00308.1.

[45] W. C. Skamarock et al., "A description of the advanced research WRF version 2," Nat. Center Atmos. Res., Boulder, CO, USA, Rep. NCAR/TN-468+STR, 2005.

[46] G. Thompson, P. R. Field, R. M. Rasmussen, and W. D. Hall, "Explicit forecasts of winter precipitation using an improved bulk microphysics scheme. Part II: Implementation of a new snow parameterization," *Monthly Weather Rev.*, vol. 136, no. 12, pp. 5095–5115, Dec. 2008, doi: 10.1175/2008MWR2387.1.

[47] M. J. Iacono, J. S. Delamere, E. J. Mlawer, M. W. Shephard, S. A. Clough, and W. D. Collins, "Radiative forcing by long-lived greenhouse gases: Calculations with the AER radiative transfer models," *J. Geophys. Res., Atmos.*, vol. 113, no. D13, Jul. 2008, Art. no. D13103, doi: 10.1029/2008jd009944.

[48] P. A. Jiménez, J. Dudhia, J. F. González-Rouco, J. Navarro, J. P. Montávez, and E. García-Bustamante, "A revised scheme for the WRF surface layer formulation," *Monthly Weather Rev.*, vol. 140, no. 3, pp. 898–918, Mar. 2012, doi: 10.1175/mwr-d-11-00056.1.

[49] N. M. Tewari et al., "Implementation and verification of the unified NOAH land surface model in the WRF model (formerly paper number 17.5)," in *Proc. 20th Conf. Weather Anal. Forecasting/16th Conf. Numer. Weather Predict.*, vol. 14, Seattle, WA, USA, 2004, pp. 11–15.

[50] S.-Y. Hong and J.-O. J. Lim, "The WRF single-moment 6-class microphysics scheme (WSM6)," *Asia–Pacific J. Atmos. Sci*, vol. 42, no. 2, pp. 129–151, 2006.

[51] G. A. Grell and S. R. Freitas, "A scale and aerosol aware stochastic convective parameterization for weather and air quality modeling," *Atmos. Chem. Phys.*, vol. 14, no. 10, pp. 5233–5250, May 2014, doi: 10.5194/acp-14-5233-2014.

[52] S. Saha et al., "The NCEP climate forecast system version 2," *J. Climate*, vol. 27, no. 6, pp. 2185–2208, Mar. 2014, doi: 10.1175/JCLI-D-12-00823.1.

[53] X. Yan, Y. Liu, Y. Xu, and M. Jia, "Multistep forecasting for diurnal wind speed based on hybrid deep learning model with improved singular spectrum decomposition," *Energy Convers. Manage.*, vol. 225, Dec. 2020, Art. no. 113456.

[54] X. Liu, J. Sun, Q. Zhang, Z. Wang, and Z. Xu, "Learning to learn evolutionary algorithm: A learnable differential evolution," *IEEE Trans. Emerg. Topics Comput. Intell.*, vol. 7, no. 6, pp. 1605–1620, Dec. 2023.

[55] Y. Sun et al., "Vertical dependency of aerosol impacts on local scale convective precipitation," *Geophys. Res. Lett.*, vol. 50, no. 2, Jan. 2023, Art. no. e2022GL102186.

[56] H. Zhao, S. Yang, Q. Wu, L. Chen, P. Zhang, and R. Li, "Supplementary data for 'convolutional neural network heating (CNNH) algorithm to remote sense latent heating rate profiles from satellite,"' Zenodo, Geneva, Switzerland, Rep. 12531329, 2024, doi: 10.5281/zenodo.12531329.

Hongwei Zhao received the Ph.D. degree in resources and environment from the School of Earth and Space Sciences, University of Science and Technology of China (USTC), Hefei, China, in 2023.

She is currently a Post-Doctoral Researcher with the School of Earth and Space Sciences, USTC. Her research interests include exploring retrieval algorithms for precipitation and latent heat based on artificial intelligence methods.

Shuping Yang received the B.S. degree in atmospheric science from the University of Science and Technology of China (USTC), Hefei, Anhui, China, in 2017, where he is currently pursuing the Ph.D. degree with the School of Earth and Space Sciences.

His research interests include 3-D precipitation retrieval and the evolution of mesoscale convective systems.

Qiong Wu received the M.Sc. degree in atmospheric science from Chinese Academy of Meteorological Sciences, Beijing, China, in 2012, and the D.Sc degree in atmospheric physics and atmospheric exploration from the Institute of Atmospheric Physics, Chinese Academy of Sciences, Beijing, China, in 2019, where she is currently responsible for the L2 product of FY-3G PMR.

Her research interests include spaceborne radar simulation, rain and cloud parameter retrieval, and ground validation.

Lin Chen received the Ph.D. degree from the Institute of Atmospheric Physics, Chinese Academy of Sciences, Beijing, China, in 2009.

Since 2009, he was with the National Satellite Meteorological Center, China Meteorological Administration (NSMC/CMA), Beijing. He was a Senior Visiting Scientist at the European Organization for the Exploitation of Meteorological Satellites (EUMETSAT), Darmstadt, Germany, from December 2014 to April 2015. Currently, he is a Senior Scientist with NSMC/CMA, the Vice Chief Engineer of FY-3 Rainfall Mission Satellite Ground Segment, and the Vice Chief Director of the Satellite Meteorology Department, NSMC. He is a member of the Global Space-based Inter-Calibration System (GSICS/WMO) and a member of WMO SDS-WAS Regional Steering Group (RSG) for Asia. He has participated in the development of ground segment for China's Fengyun-2, Fengyun-3, and Fengyun-4 meteorological satellites. At present, he is leading a team to develop the Fengyun satellite climate dataset and the next-generation carbon satellite ground system in China. He has authored or co-authored over 80 science papers in peer-reviewed journals. His research interests include sensor development and design on the polar orbit satellite and cal/val activities of meteorology satellites and remote sensing scientific products retrieval as well as their climate effect and applications.

Peng Zhang (Senior Member, IEEE) was born in Shaanxi, China, in 1970. He received the Ph.D. degree in atmospheric physics from the Institute of Atmospheric Physics, Chinese Academy of Sciences (IAP/CAS), Beijing, China, in 1998.

He was with the Earth Observation Research Center, National Space Development Agency of Japan (EORC/NASDA), Tokyo, Japan as a postdoctororal position, from 1998 to 2001. He was with the National Satellite Meteorological Center, China Meteorological Administration (NSMC/CMA), Beijing, from 2001 to 2023 and was the Deputy Director-General, from 2013 to 2023. He was a Visiting Scholar at the Center de Meteorologie Spatiale, Meteo-France (CMS/Meteo-France), in 2003 and a Visiting Associate Scientist at the Cooperative Institute for Meteorological Satellite Studies, Space Science and Engineering Center, University of Wisconsin–Madison (CIMSS/SSEC/UW-Madison), in 2005. He has been the Director-General of CMA Meteorological Observation Centre (MOC), since 2023. Currently, he is the Chief Scientist of Chinese Polar-Orbiting Meteorological Satellite Program, and his major fields cover the atmospheric remote sensing, satellite calibration and validation, and atmospheric radiative transfer calculation. He has authored and co-authored more than 200 articles published in refereed scientific journals to date.

Rui Li received the Ph.D. degree in atmospheric science from the School of Earth and Space Sciences, University of Science and Technology of China (USTC), Hefei, China, in 2005.

He was a Post-Doctoral Researcher and a Full Research Scientist at the State University of New York, Albany, NY, USA, from 2006 to 2009 and 2009 to 2013, respectively. Since 2013, he has been a Professor at USTC. He is currently the Deputy Dean of the School of Earth and Space Sciences at USTC, an Adjunct Researcher at the Deep Space Exploration Laboratory, an Adjunct Professor at the State Key Laboratory of Fire Science, and the Director of the CMA-USTC Laboratory of Fengyun Remote Sensing. His primary research is concentrated on the carbon and water cycles and energy balance processes within the climate system, and he is dedicated to the advancement of sophisticated multi-source satellite remote sensing algorithms and datasets. His recent research has particularly emphasized the use of active and passive microwave remote sensing to investigate key parameters in land-atmosphere interactions, such as precipitation, latent heat, evapotranspiration, and gross primary productivity (GPP). He is also committed to the application of multi-source satellite remote sensing products in climate system research.

Dr. Li has authored more than 100 articles in academic journals, including *NSR*, *RSE*, *npj CAS*, *ACP*, *JGR*, and IEEE TRANSACTIONS ON GEOSCIENCE AND REMOTE SENSING.